Available online at www.sciencedirect.com
ScienceDirect
Earth and Planetary Science Letters 255 (2007) 324–338
EPSL
www.elsevier.com/locate/epsl

Slab surface temperature in subduction zones: Influence of the interplate decoupling depth and upper plate thinning processes

D. Arcay [a,*], E. Tric [a], M.-P. Doin [b]

[a] Université de Nice-Sophia Antipolis, Laboratoire Géosciences Azur, 250 r. Albert Einstein, 06560 Valbonne, France
[b] Ecole Normale Supérieure, Laboratoire de Géologie, 24 r. Lhomond, 75231 Paris Cedex 05, France

Received 20 June 2006; received in revised form 12 December 2006; accepted 22 December 2006
Available online 12 January 2007
Editor: C.P. Jaupart

Abstract

The thermal state of the top of the subducting plate is strongly affected by the mantle wedge flow structure. We identify three main factors controlling the influence of the corner flow on the slab surface temperature: (1) the mantle rheology, (2) the interplate decoupling depth, and (3) the intensity of thermomechanical ablation of the overriding plate. The first two factors are discussed using results from published simulations. We perform 2D numerical simulations of mantle wedge flow to assess the role of the third factor. The non-Newtonian rheology depends on temperature, pressure, yield stress, and composition. The thermochemical convection code includes a water transfer model and the water weakening effect on mantle rocks. Slab dehydration triggers water saturation of the overlying mantle wedge and upper plate. When weakening of mantle rocks by hydration is included in the simulations, the interplate decoupling depth decreases and the upper plate thermal thinning increases. A relatively cold blanket develops on top of the slab below the interplate decoupling depth. Cold materials removed from the thinned upper plate are advected by the corner flow and are accreted to the viscous layer dragged along the slab surface. As a result, the thickness of the insulating layer covering the slab surface increases with the water weakening effect, together with the upper plate thermal thinning rate.

Pressure–temperature (P−T) paths followed by crustal rocks during subduction quantify the influence of upper plate thinning processes on the slab surface thermal state. The slab surface temperature below 100 km can be lowered by as much as 130 °C due to increased thermal convection at the base of the upper plate. At shallower depths (<100 km), this effect competes with the heating of the slab induced by a shallowing of the interplate decoupling depth. For a small water weakening effect, the enhanced corner flow mainly yields a shallow decoupling depth and warms the slab top from 50 to 100 km. For a large weakening effect, the slab surface is cooled by convective drips detaching from the overriding lithosphere that counter-balance the effect of a shallow decoupling depth. P−T paths in case of efficient upper plate thinning are thus inferred to be uniformly colder than predicted from the slab thermal parameter (age × velocity) and non-Newtonian wedge rheology.

Keywords: subduction; mantle wedge; slab thermal state; rheology; water weakening

1. Introduction

The thermal state of the subducting slab top is a key issue in understanding slab dehydration and island arc volcanism. In particular, the conditions for which the

* Corresponding author. Now at Institute of Geophysics, Swiss Federal Institute of Technology (ETH-Zürich), CH-8093 Zürich, Switzerland. Tel.: +41 44 633 29 07; fax: +41 44 633 10 65.
E-mail addresses: diane.arcay@erdw.ethz.ch (D. Arcay), tric@geoazur.unice.fr (E. Tric), doin@geologie.ens.fr (M.-P. Doin).

0012-821X/$ - see front matter © 2007 Elsevier B.V. All rights reserved.
doi:10.1016/j.epsl.2006.12.027

slab surface temperature (hereafter called SST) is large enough to trigger sediment melting remain unclear [1]. The geochemistry of arc basalts is explained by the contribution of two components, a major mantle wedge source and a volatile flux derived from subducted sediments and oceanic crust (e.g., [2–4]). Partial melting of the subducted metasediments, recycling highly incompatible elements, as Th and Be, could be a common feature of subduction, and would not be restricted to slow subduction of young lithospheres ([1], and references therein). Another debated question relies on the upper lithosphere structure in the volcanic front area. The temperature at the base of the arc crust is often inferred from magmatic and metamorphic studies to be particularly high [5]. The last equilibration between the basaltic liquid and the surrounding peridotite was suggested to take place at 1300–1450 °C and 30 to 65 km depth, depending on local water contents and magma composition (e.g., [6–10]). Furthermore, exposed arc sections, the Kohistan section in Pakistan [11,12] and the Talkeetna section in Alaska [13], display very high grade metamorphic rocks indicating temperature near 1000 °C at the base of the arc crust.

Numerical models of subduction predict that the slab temperature structure mainly depends on the slab thermal parameter (convergence rate × age, [14–17]). However, the SST is also highly sensitive to the mantle wedge dynamics and the interplate decoupling depth. The interplate decoupling depth corresponds to the depth where the mantle above the subducting lithosphere becomes mechanically coupled to the slab and is carried along with it ([18], Fig. 1). The flow structure in the mantle wedge can lead to a significant thermal thinning of the upper lithosphere in the backarc region if the mantle strength is locally decreased by slab dehydration [19,20], which in turn might modify the SST in the vicinity of the interplate decoupling depth. Numerical modelling of subduction as well as the mantle wedge tip thermal and flow structure remains a sensitive issue, because of very high gradients of temperature, strain rate, and strength. The study of the mantle wedge tip is further complicated by the coupling between plate tectonics and mantle convection. In some studies of convergence zones, plate deformation [21] and lithosphere/asthenosphere interactions [22–24] are not modelled together. Moreover, the subduction zone dynamics is controlled by the rheology of the different lithological layers forming the subducting slab (sediments/oceanic crust/mantle), which adopt various rheological behaviors (elastic/brittle/viscous) as a function of pressure, temperature, composition, and strain rate. As a result, complex subduction processes are simplified in numerical simulations. Modelling strategies significantly affect the obtained temperature and flow structure, which partly explains why numerical simulations do not predict whether the subducted crust should melt or not [25]. We start this paper by a discussion about how modelling choices and approximations may affect the slab surface thermal state. Then, we present the thermomechanical simulations of subduction and wedge flow, that include first, a water transfer model as a function of slab dehydration and mantle wedge hydration reactions, and second, a model where mantle rheology depends on water content [19]. We quantify the interplate decoupling depth variations as a function of the mantle wedge flow structure, and show how it affects the SST. We show that a strong warming and thinning of the overlapping lithosphere does not result necessarily in a SST increase, but that it may even yield a significant cooling.

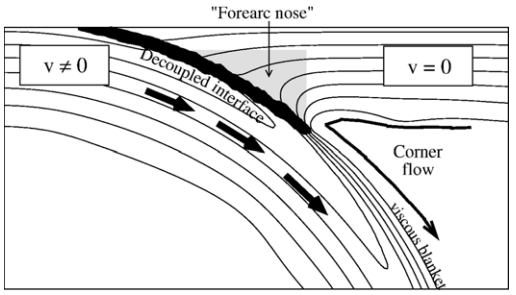

Fig. 1. Sketch of the mantle wedge structure and definition of the interplate decoupling depth. Isotherms (black lines) are displayed every 150 °C.

2. Factors influencing the slab surface thermal state

Before presenting our numerical simulations, we summarize how the design of subduction numerical simulations and input parameters affect the wedge flow and slab temperature (see also [25]), as illustrated in Figs. 1 and 2. The temperature evolution in the wedge is governed by the balance between conductive cooling from the slab (also called a “heat sink”) and advection of warm asthenospheric rocks into the wedge by the return flow. This rising return flow is mainly a passive flow, and occurs to replace the mantle dragged down along the slab by viscous coupling across the slab top (“corner flow” on Fig. 1). Therefore, a fundamental feature of subduction is the coupling across the slab surface, which is controlled by [1] the strain localization along the slab/upper plate interface, and [2] the temperature and stress dependence of the ductile rheology. We will detail below these two effects. A complete discussion of the fault parameterization influence can be found in [25].

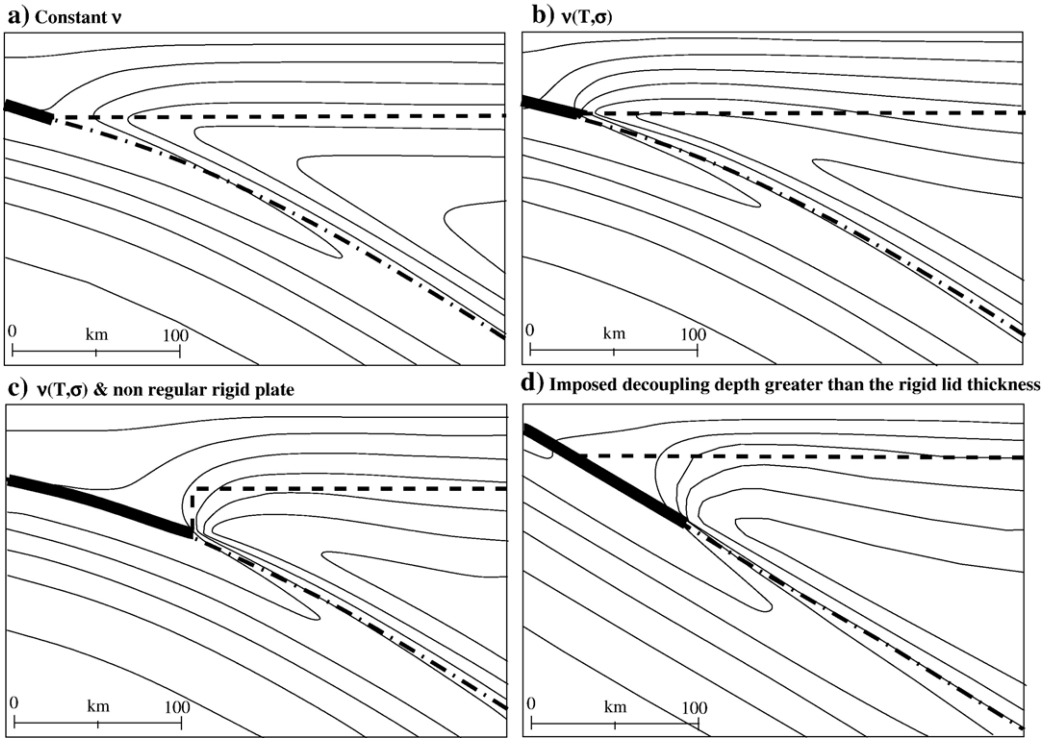

Fig. 2. Influence of the rheology and boundary conditions on the mantle wedge flow structure. (a, b, and c) Modified after [35], (d) modified after [36]. The thin solid lines represent isotherms every 200 °C. The dashed line is the base of the prescribed rigid domain within the upper plate. The slab surface is shown by a dot-dashed line and the decoupled interplate plane is shown by a thick solid line. Panel (a): isoviscous rheology. Panel (b–d): temperature- and stress-dependent rheology.

2.1. Influence of the interplate boundary modelling

Numerical experiments with a viscous temperature-dependent rheology fail to produce strain localization along the subduction plane, but instead lead to a stagnant lid at the surface (e.g., [26]). Therefore, strain localization is most often obtained by modelers by assigning weak nodes on a prescribed subduction plane, with a decreased viscosity [27,1], or a low tangential stress [28–30], or by imposing kinematically the convergent velocity field in the upper plate and subducting slab [18,17,31], see Fig. 2. In both cases, this corresponds to prescribing the interplate decoupling depth (Fig. 1) that must be tested as an extra subduction parameter [18].

A common feature of all simulations cited above with a prescribed decoupling depth and a temperature-dependent viscosity is that the tip of the hot mantle wedge moves upwards and towards the trench until reaching the base of the decoupling interface: Hot rising material replaces there the mantle material which is dragged down by the slab directly below the decoupling interface (e.g., [18], Fig. 2b–d). Below the forearc, the cold wedge (also called "cold forearc nose", Fig. 1) extends until the tip of the decoupling interface, where isotherms become more or less vertical. Consequently, focused strain rate, confined in the decoupling interface until its base, jumps away from the slab surface and reaches the asthenospheric wedge over a relatively narrow interval where thermal gradients are very high. This area corresponds to a strong increase in SST [31,25,19]. At the surface, the simulated heat flow remains low above the forearc nose, and increases rapidly on top of the decoupling depth tip [18].

When the "fault" (defined as a weak plane) is ignored, leading to a complete viscous coupling between the two converging plates, one obtains unrealistic deformation of the overlying plate by either extreme ablation or recycling [25]. For a prescribed subducting plate velocity and a no-slip condition on top of the upper plate, the wedge tip rises to the surface, as would be obtained when setting a very shallow decoupling depth [32]. For a free-slip boundary condition on top of the upper plate, the latter deforms as it is dragged along with the subducting plate leading to a particularly cold slab surface [33].

Constraints on the thermomechanical structure in the vicinity of the decoupling depth are given by seismic

attenuation studies, indicating that the transition between a hot mantle area and the forearc nose could be sharp and vertical [25,34,35]. Such a feature appears in numerical simulations with temperature-dependent viscosity when the decoupling depth exceeds the imposed rigid lid thickness ([36,27,35], Fig. 2c,d). However, it is much less clear when the decoupling depth is equal to the rigid lid thickness (Fig. 2b).

In the latter case, the prescribed rigid lid then partly includes the high temperature low viscosity wedge, which should normally flow, leading to erroneous wedge tip structure (Fig. 2b). This is why a vertical interface between the mobile wedge and the overlying rigid plate is sometimes imposed (as shown in Fig. 2c, [37,31,35]).

These models allow one to reproduce the "cold forearc nose", observed by seismic attenuation tomography, and the surface heat flow variations, by adjusting the prescribed geometry of the decoupling interface and rigid lid. However, physical modelling of the mantle wedge–slab coupling may rely on the computation of the brittle–ductile transition along the subduction plane [25].

2.2. Isoviscous rheology versus temperature-dependent viscosity

Three main models of mantle rheology are used in corner flow simulations: constant viscosity, temperature-dependent strength, and temperature- and stress-dependent rheology. For an isoviscous mantle wedge, the return flow includes as much cold material from the base of the overriding lithosphere as hot material from the asthenosphere (both have the same viscosity). The corner flow is therefore uniform and horizontal below the overlying rigid plate [31,1,5], Fig. 2a). This prevents any local upper plate thinning. Furthermore, the cold material from the upper plate base, constantly advected downwards, thermally insulates the slab surface from the hot asthenosphere (Fig. 2a). Hence the SST remains low without any increase around the decoupling depth [1], and cannot account for the strong surface heat flow increase between the forearc region and the volcanic front [18]. Such a model does not yield SST high enough to reach partial melting conditions below the volcanic front [31].

On the contrary, a temperature-dependent viscosity favors a focussing of the mantle return flow in a hot wedge tip and, locally, a strong increase of the SST ([18,1,5], Fig. 2b), because it decreases the cold material amount of the upper plate base accreted to the thermal boundary layer forming at the slab surface (also called "viscous blanket", [27], Fig. 1) (compare Fig. 2a and b), so the SST remains hotter during the slab descent. However, the absence of cold material advection by the wedge flow at a large distance from the trench below the backarc inhibits any distributed lithospheric thinning. Hence, a mantle wedge model including a temperature-dependent viscosity cannot explain high surface heat flow several hundreds of kilometers away from the volcanic front, as observed in the Cascadia subduction zone [5].

In the case of a non-Newtonian rheology, the wedge tip appears to be more focussed than for a Newtonian rheology. Effective viscosities are indeed relatively lower at the decoupling interface tip, where strain rates are higher, than further away from it, enhancing corner flow localization ([38,18,31,5,35], Fig. 2b). As a result, the slab surface temperature is increased by 150–225 °C in the vicinity of the decoupling depth [31,25].

2.3. Subduction model used in this study

Our subduction model differs in some respects from the models discussed above. First, the decoupling interface geometry is not fixed by mechanical boundary conditions, nor dependent on assigned weak nodes along the interplate, but it is here provided by the free advection of a weak crustal layer along the subducting plane. The dominant mechanical behavior (pseudobrittle or viscous) is controlled by temperature, pressure, and deformation rate, and differs in the crust and the mantle. As a result, the interplate decoupling depth is free to evolve along with the temperature structure. Second, the subducting slab geometry evolves freely in the interplate vicinity as well as in the asthenosphere and deeper mantle, because the imposed kinematic condition forcing convergence is located far away from the trench. Third, the overlying plate rigidity is here only insured by the intrinsic stiffness of cold mantle rocks. Therefore, thinning of the upper lithosphere is possible, due to a combination of flow in the more ductile (hot and/or hydrated) part of the lithosphere and upwards heat conduction, since no kinematic nor mechanical condition is prescribed across the lithosphere. Finally, in our simulations, as in [1], the wedge flow is driven both by subducting plate motion, and by thermal buoyancy. The latter will yield thermal convection in the wedge, which can be related to thermal boundary layer instabilities in a temperature-dependent viscosity fluid [39–41].

Performing a dynamic model of subduction allows simulation of the physical mechanisms that fix the interplate decoupling depth at equilibrium. However, the complexity and large degree of freedom of a dynamic model prevent the simulated subduction

geometry from being a priori controlled. Therefore, this strongly limits comparison between observations and dynamic model predictions. This comparison is more fruitful using prescribed slab/overriding plate interface, as is done in many studies cited above.

3. Numerical setup

To simulate subduction, we use a thermochemical code of convection [42,43] that solves the momentum, energy, and mass conservation equations. We assume incompressibility, except for the thermal buoyancy term in the momentum equation, and the adiabatic heating term in the energy equation (extended Boussinesq approximation). Shear heating and uniform heat production are also included in the heat conservation equation. The oceanic crust and the mantle are tracked by two kinds of tracers that differ by their density and rheology. The buoyancy depends on temperature (through the thermal expansion coefficient) and composition (crust/mantle). Compositional tracers are advected with the velocity field [44].

Petrogenetic grids appropriate for both crust and mantle are used to compute the water content evolution. We do not include changes in density with varying water content and metamorphic grade. Subducting crust eclogitization or mantle slab hydration produce strong and competing effects on the slab pull, thus adding a new complexity to the slab dynamics and slab dip. In this simplified study, we neglect these effects to focus on the mantle wedge flow driven only by slab dehydration and thermal buoyancy.

We first present boundary conditions and subduction geometry. The water transfer model and the rheology are then briefly described. A discussion of the different model assumptions can be found in [19]. Parameters are all given in Table 1.

Table 1
Thermomechanical parameter names and values

Parameter name	Symbol	Value
Box height	H_0	555 km
Bottom temperature	T_b	1888 K
Surface temperature	T_s	273 K
Mantle density	ρ_m	3300 kg m^{-3}
Crustal density	ρ_c	2920 kg m^{-3}
Mantle radiogenic heat production	A	9.20×10^{-8} W m^{-3}
Adiabatic gradient	$\left(\frac{\partial T}{\partial z}\right)_{\text{adiab}}$	0.445 K km^{-1}
Thermal diffusivity	κ	0.8×10^{-6} m^2 s^{-1}
Thermal expansion coefficient	α	3.5×10^{-5} K^{-1}
Heat capacity	C_p	0.971×10^{3} J $(K\ kg)^{-1}$
Gravity acceleration	g	9.81 m s^{-2}
Oceanic crust thickness	H_c	7 km
Preexponential constant, "dry" viscous rheology	A_0^{dry}	53,280 Pa $s^{\frac{1}{3}}$
Activation energy in the mantle	E_a^m	395 kJ mol^{-1}
Activation energy in the crust	E_a^c	285 kJ mol^{-1}
Activation volume	V_a	2.34×10^{-5} m^3 mol^{-1}
Cohesive strength	τ_0	1 MPa
Stress exponent in the viscous rheology	n	3
Stress exponent in the brittle rheology	n_p	30
Reference strain rate	$\dot{\varepsilon}_{\text{ref}}$	10^{-14} s^{-1}
Yield stress increase with depth (crust)	γ_c	0.06
Yield stress increase with depth (mantle)	γ_m	1.5
Hydrous strength reduction	f_v	1–100
Convergence rate	v	2–10 cm/yr

3.1. Mechanical and thermal conditions

To mimic plate convergence, a constant velocity is imposed on the top left part of the subducting plate, on a 16 km thick layer (Fig. 3a), far away from the subduction zone. Free slip is applied on the remaining surface, 280 km before the initial trench location on the subducting plate, and on the overriding plate. Before subduction initiation, a 7 km thick crustal layer covers the subducting lithosphere, prograding into a 30° dipping plane, until 55 km depth. The crustal strength is assumed to be extremely low with respect to the mantle strength. When convergence is initiated, the deformation localizes along the weak dipping plane and the lithosphere bends. As convergence proceeds, the initial subduction plane is continuously filled by the weak crustal tracers covering the subducting lithosphere. This allows maintenance of deformation localization and sustains the subduction process [45]. Other thermal and mechanical boundary conditions are displayed in Fig. 3a.

At subduction onset, the lithosphere has a quite homogeneous thickness of 100 km. This thermal structure results from the statistical thermal equilibrium between the convective upwards heat transfer and the surface conductive cooling, computed with the same boundary conditions as described above, but without convergence velocity. Perturbations of the thermal lithosphere base are due to small-scale convection (Fig. 3). The set of boundary conditions is slightly changed (depicted on Fig. 3b) to perform long-term simulations, requiring a subduction length larger than 1100 km: [1] the side by which the subducting plate enters the simulation box is open, while [2] we impose along this side a constant horizontal thermal gradient.

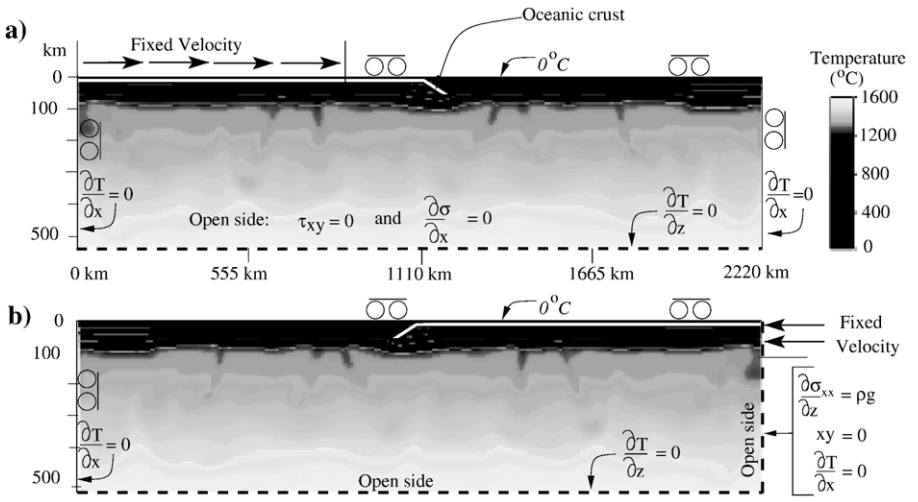

Fig. 3. Boundary conditions and initial state before subduction initiation. Isotherms (white thin lines) are displayed every 300 °C. The thick white line represents the oceanic crust at the subducting plate surface. Panels (a) and (b) show the two different setups used in this study.

3.2. Water transfer model

3.2.1. Water content as a function of pressure and temperature

Water transfers are a function of dehydration and hydration metamorphic reactions, i.e., they depend on hydrated mineral stability domains. In our model, the water transfer computation is based on two phase diagrams, excluding here mineral metastability, and valid for a lherzolite for mantle tracers [46] and for a gabbro for crustal tracers [47]. The initial oceanic crust water content is set to 2.97 wt.%, the saturation value of a gabbro composition in the greenschist facies [47]. Part of the lithospheric mantle underlying the oceanic crust is initially fully serpentinized (6.5 wt.% of water) over a 15 km thick layer. This simple hydration structure before subduction accounts both for the hydroalteration of peridotite near the mid-oceanic ridge, and for deep metasomatism that may occur along normal faults in the region where the subducting lithosphere bends near the trench [48–53].

In the P−T domain corresponding to asthenospheric conditions, where nominally hydrous minerals are not stable, peridotite minerals absorb a few hundred ppm in weight of water [54–56]. Below wet solidus, water amount at saturation is taken as that dissolved by a lherzolite at 1000 °C, using water solubilities measured by Kohlstedt et al. [57], Lu and Keppler [58], and Rauch and Keppler [59], respectively, in olivine, pyrope, and clinopyroxene, respectively. The water amount dissolved by peridotite increases with pressure. Its minimum value is ~390 ppm at 70 km depth [19]. In the wet partial melting domain, the water content is assumed to decrease linearly with temperature from its value at the wet solidus to zero at the dry solidus [60].

3.2.2. Water transfer computation

To compute water transfers, the mantle wedge area is further divided into 1.4×2.8 km^2 cells, containing on average four tracers. At each time step, the water content at saturation is calculated for all tracers inside the mantle wedge as a function of pressure, temperature, and composition (crust or mantle) using phase diagrams. If the former water content of a tracer is larger than that at saturation, the tracer undergoes a dehydration reaction, and its water in excess is released. If possible, the "free" water is first absorbed by nearby undersaturated tracers, i.e. those located in the same cell. If left, the remaining free water amount is redistributed to undersaturated tracers located in the above adjoining cell. Unabsorbed water migrates progressively upwards cell by cell, until exhaustion or until it reaches the depth of 11 km, where it is extracted from the simulation box. Therefore, the water expelled by dehydration migrates vertically and instantaneously until being completely absorbed.

3.3. Rheology model

The simulated rheology is a function of temperature, T, pressure, P, strain rate, $\dot{\varepsilon}$, composition, C (crust or mantle), and water content. An effective viscosity, ν, is defined through the relationship: $\tau = \nu\dot{\varepsilon}$, where τ and $\dot{\varepsilon}$ are the second invariants of the stress and strain rate tensors, respectively. The effective viscosity is given by the

inverse average between a brittle-plastic term, ν_b, and the non-Newtonian viscosity strength, ν_v, $\nu^{-1}=\nu_b^{-1}+\nu_v^{-1}$.

The brittle-plastic rheology is implemented through a yield stress, τ_y, relationship with depth, z: $\tau_y=\tau_0+\gamma(C)\rho gz$, where τ_0 is the cohesive strength at the surface, and γ the yield stress increase with depth depending on rock composition and related to the friction coefficient, f_s [61].

The effective plastic viscosity, ν_b, is: $\nu_b = \tau_y \left(\dot{\varepsilon}^{\frac{1}{n_p}-1}\right)/\left(\dot{\varepsilon}_{ref}^{\frac{1}{n_p}}\right)$, where $\dot{\varepsilon}_{ref}$ is a reference strain rate and n_p is a large stress coefficient (Table 1). In the brittle-plastic domain, we then obtain very large strain rates as soon as stress exceeds the yield stress. The non-Newtonian rock viscosity, ν_v, writes as:

$$\nu_v = A_0([OH^-])\exp\left(\frac{E_a(C)+V_a\rho gz}{nRT}\right)\dot{\varepsilon}^{\frac{1}{n}-1} \quad (1)$$

where E_a is the activation energy (depending on composition), V_a is the activation volume, n is an exponent different from 1, and R is the gas constant (Table 1). The values chosen for thermomechanical parameters are discussed in [19]. In the present case, a temperature increase of 100 °C at 1200 °C and 100 km depth yields an effective viscosity decrease by a factor ~16 at a constant strain rate.

The values we choose for both the crust friction coefficient, f_s, and the crust activation energy, E_a, $f_s^c=0.05$ and $E_a^c=285$ kJ mol^{-1}, are low compared to their mantle equivalents ($f_s^m=0.6$ and $E_a^m=395$ kJ mol^{-1}). Therefore, the modelled oceanic crust is weaker than mantle rocks in the viscous as well as in the plastic domain.

Rock strength in wet conditions is strongly decreased, even for very low amounts of water [62,63]. We include the water weakening effect in our simulations by an ad-hoc decrease of the preexponential factor, A_0, in Eq. (1), as a function of $[OH^-]$:

$$A_0([OH^-]) = A_0^{dry}\left(\left[1-\frac{1}{f_v}\right]\exp\left(-\frac{[OH^-]}{[OH^-]_0}\right)+\frac{1}{f_v}\right) \quad (2)$$

where A_0^{dry} is the preexponential factor in the Arrhenius law (Eq. (1)) for a dry rock, $[OH]_0^-$ is a reference water content, set to the amount dissolved by peridotite at the lithosphere/asthenosphere boundary (620 ppm in weight), and f_v is the maximum hydrous strength reduction. Values of f_v between 1 and 100 are here tested.

The arbitrary relationship (2) assumes that the water weakening effect is clearly smaller when water is only dissolved within anhydrous minerals than when nominally hydrous minerals are formed. For water content lower than 0.42 wt.% ($[OH^-]\lesssim 7[OH^-]_0$), the strength reduction given by Eq. (2) increases with water content, but remains always much lower than the maximum value f_v. On the contrary, the strength reduction when hydrous minerals are present ($[OH^-]\gg[OH^-]_0$) is very close to f_v. Thus, we assume that the formation of hydrous minerals, such as amphibole, chlorite, and serpentine, by more than 10 wt.%, strongly weaken bulk peridotite. This is suggested by the observation of strain localization within hydrated layers in natural mafic rocks [64,65]. However, we are not aware of laboratory experiments quantifying the mantle strength reduction associated with the nominally hydrated phase formation. Water weakening in the hydrated crust is not included, to keep the same interplate properties along the subduction plane.

3.4. Numerical resolution

The conservation equations are solved with a finite element method on a non-deforming grid (Eulerian approach, [42,43]. The simulation box, 2220 km wide and 555 km high (Fig. 3) is discretized into 332×90 nodes. The grid is refined to improve resolution in areas of high thermal and deformation gradients. Close to the subduction plane and in the wedge tip area, the horizontal and depth grid spacings are 2.8 and 2.3 km, respectively. Outside the mantle wedge area, they are equal to 9.5 and 10.2 km, respectively. The tracer density is uniform over the simulation box (1 per km^2), with a minimum of 7 tracers in the smallest meshes. A simulation with two tracer per km^2 shows that the influence of tracer density, as estimated by global parameters (e.g., average temperature), as well as local values (e.g., wedge tip temperature), is always smaller than 1.7% [19]. The numerical discretization used here was also validated in a previous study [19].

4. Results

We present in the next subsection how water weakening modifies the thermo-mechanical structure of the mantle wedge. We then describe how the maximum extent of the decoupling interface evolves as a function of the convergence rate and the hydrous strength reduction, before studying the SST evolution.

4.1. Mantle wedge flow for a water weakening rheology

In our simulations, the subducting plate dehydration corresponds to [1] the oceanic crust eclogitization at

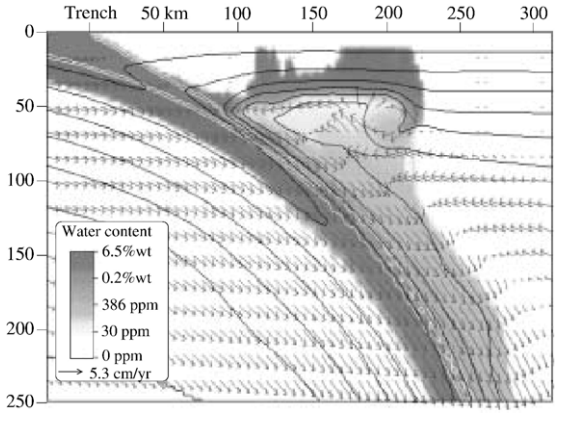

Fig. 4. Zoom on the subduction zone structure 13.5 Myr after subduction initiation, for a maximum hydrous strength reduction, f_v, equal to 50 (simulation S5, Table 2). Isotherms (black lines) are displayed every 200 °C. The white line delimits the oceanic crust.

depths shallower than ~80 km, and [2] the progressive dehydration of the serpentinite layer located under the crust. The water released by deserpentinization, between 100 and 200 km depth, almost instantaneously water-saturates the overlying asthenosphere that dissolves less than 1000 ppm in weight of water (Fig. 4). The remaining water then progressively hydrates the upper lithosphere, at which base the water is absorbed in nominally anhydrous minerals. At shallower depths, hydrated minerals form, such as amphibole, talc, antigorite and chlorite ([19], Fig. 5). The water weakening factor, f_v, is progressively increased from simulations S1 to S6, between 1 and 100 (Table 2).

The flow and temperature structures for a passive hydration process ($f_v = 1$) are illustrated in Fig. 6a. They present similar features as those described previously (Section 2 and Fig. 2), however the decoupling depth equilibrates at relatively large depth (~100 km) and the return flow does not seriously erode the overlying lithosphere. When hydration decreases the mantle rock strength ($f_v > 1$), asthenospheric corner flow and upper lithosphere thinning near the subduction plane base are enhanced ([20], Fig. 6a). The return flow then includes an increased amount of cold material originating from

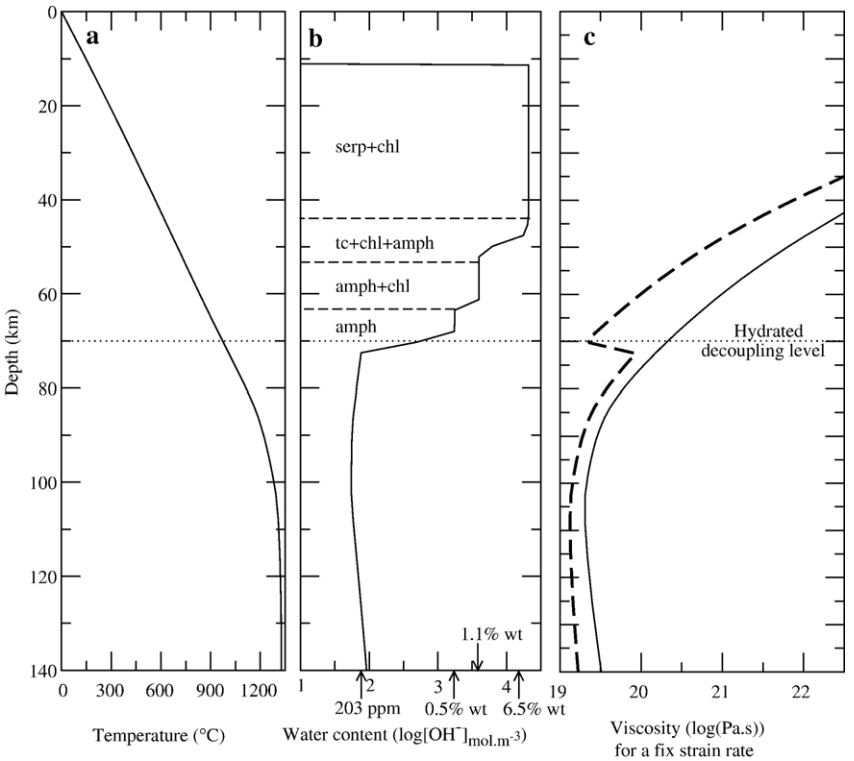

Fig. 5. Profiles across the overlying plate at subduction initiation. Panel (a): Thermal profile. Panel (b): water content profile computed with the temperature profile in panel (a) and the phase diagram for lherzolite from [46]. Thin dashed lines delimit depth intervals where nominally hydrated minerals are stable at water-saturation condition (amph: amphibole; chl: chlorite; tc: talc; serp: serpentine). Panel (c): Strength profiles for two values of the hydrous strength reduction, f_v, for a fix strain rate ($\dot{\varepsilon} = 10^{-14}$ s^{-1}), and for thermal and water content profiles displayed in panels (a) and (b). Thin solid line: reference case, $f_v = 1$; thick dashed line: $f_v = 50$. Below the "weak level", the strength reduction depends on f_v and the dissolved water amount. At shallower depths, due to the presence of hydrous minerals, the strength reduction is larger and equal to f_v.

Table 2
Simulation list

Simulation	Subduction rate (cm/yr)	Hydrous strength reduction, f_v	Effective 'wet' viscosity [a] 100 km depth (Pa s)	Viscosity at the hydrated decoupling level [b] (Pa s)
S1	5.3	1.	2.0×10^{19}	2.8×10^{20}
S1b	2.	1.	2.0×10^{19}	2.8×10^{20}
S1c	10.	1.	2.0×10^{19}	2.8×10^{20}
S2	5.3	5.	1.4×10^{19}	5.5×10^{19}
S3	5.3	10.	1.32×10^{19}	2.8×10^{19}
S4	5.3	20.	1.3×10^{19}	1.4×10^{19}
S5	5.3	50.	1.28×10^{19}	5.62×10^{18}
S6	5.3	100.	1.25×10^{19}	2.0×10^{18}
S7	5.3	50.	1.28×10^{19}	5.62×10^{18}

[a] For a fix strain rate, $\dot{\varepsilon}=10^{-14}$ s^{-1}.
[b] At $T=980$ °C and initially $z=70$ km, same constant strain rate.

the upper plate base, which is dragged along with the slab and accreted to a thickened viscous blanket.

To understand the strong thinning of the upper plate occurring for $f_v>20$ (Figs. 4 and 6a), it is important to see how hydration modifies the upper plate strength. The latter is illustrated on Fig. 5c, where the formation of amphibole at 70 km depth and ~980 °C induces a sharp strength decrease, by a factor close to f_v. If the water weakening amplitude, f_v, is greater than 20, the hydrated lithosphere at ~980 °C becomes weaker than the water-saturated asthenosphere ([20], see Table 2). The 980 °C isotherm then acts as a mechanically weak level, and favors the convective destabilization of the underlying layer, driven by its negative thermal buoyancy (Fig. 6a, $f_v=100$). This convective destabilization of the upper lithosphere base is sustained until the simulation end. The removed lithospheric volume is quite large as the upper lithosphere is eroded over its whole hydrated width (~150 km, Fig. 4). The cold blobs that detach from the lithospheric lid are taken along by the corner flow and stick on the slab surface, strongly thickening the viscous blanket that insulates the slab surface.

4.2. Interplate decoupling depth estimation

We have shown above (Section 2.1) that the interplate decoupling depth controls the location of the wedge tip. On the other hand, the return flow at the wedge tip, when focussed by temperature- and stress-dependent viscosity, carries hot material close to the slab surface. The SST increase thus promotes a shallowing of interplate decoupling depth. The interplate decoupling depth at equilibrium is then fixed by the balance between cooling by heat conduction in the forearc nose and heating by corner flow (Fig. 1). In the following, we quantify how the interplate decoupling depth varies with subduction velocity and with the overlying plate stiffness.

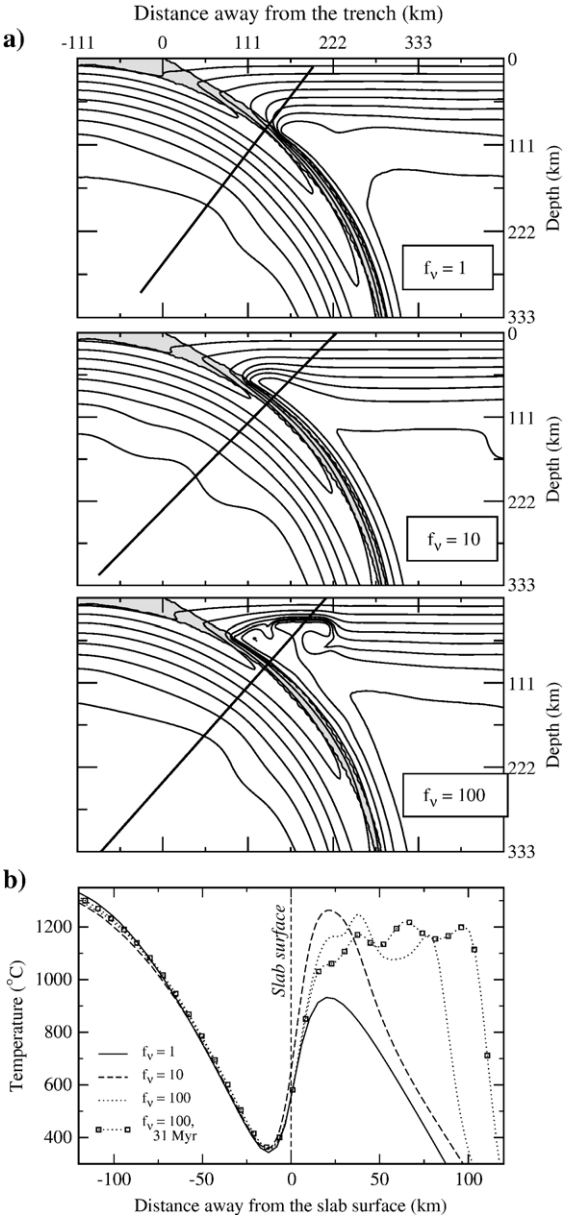

Fig. 6. Panel (a): Zoom on the subduction zone thermal structure and location of thermal profiles computed across the subducting plate, 13 Myr after subduction initiation, for three simulations: $f_v=1$ (S1), 10 (S3), and 100 (S6). Isotherms are displayed every 150 °C (thin lines). The crust is displayed in light gray. Panel (b): Corresponding thermal profiles across the subducting plate (except for simulation S6, also computed at 31 Myr). The horizontal axis origin ($x=0$) is set at the slab surface, defined as the mid-depth inside the crustal layer. Negative distances correspond to the lower side of the diving plate. Temperature oscillations observed in the mantle wedge in the $f_v=100$ case result from multiple cold blobs dripping from the upper lithosphere.

A close look at stress, strain, and dissipation energy in the subduction zone helps define the interplate decoupling depth. Maximum deformation rates, $\dot{\varepsilon}$, remain localized along the decoupled interface on the slab surface until they jump into the mantle wedge, dividing into the return flow (top branch) and the slab drag above the viscous blanket (bottom branch, Fig. 7a). The interplate decoupling depth, labelled z_{dec}, corresponds to the brittle–ductile transition along the weak subduction plane. Stress in the subduction plane increases with depth together with the yield stress, τ_y, and below z_{dec}, falls off quickly due to the crust and mantle ductile behavior and strong thermal gradients. Shear heating, $\tau\dot{\varepsilon}$, thus increases along the plate interface between the surface and z_{dec}, and falls quickly below (Fig. 7a). Here, we estimate the decoupling depth, z_{dec}, by measuring the depth where dissipation energy is maximum. Note that the shear heating here, for a friction coefficient of 0.05 in the subduction plane, is moderate and much smaller than the one that would have been obtained for a friction coefficient of 0.6–0.7.

4.2.1. Dependence of the decoupling depth in convergence velocity

We compare for convergence rates of 2, 5.3, and 10 cm/yr (simulations S1b, S1 and S1c, Table 2) the interplate decoupling depth obtained at identical subducting slab length (~745 km), without water weakening effect (f_v=1). Fig. 7b shows that the interplate decoupling depth shallows from 105 km to 82 km when the velocity increases from 2 to 10 cm/yr. This can be explained by three main processes. First, the corner flow is enhanced. Second, the dissipation heating along the subduction plane rises slightly, even if it remains low due to the low crustal friction coefficient. Third, the deformation rate increases not only along the subduction plane, but also in the mantle wedge tip (Fig. 7a). Because of the non-Newtonian rheology, this leads to a viscosity decrease in the wedge tip and enhances corner flow focussing. As a result, the convergence rate increase favors the subduction plane base warming and reduces the equilibrium depth of interplate decoupling.

4.2.2. Interplate decoupling depth as a function of the hydrous strength reduction

Fig. 7c displays the decoupling depth as a function of the hydrous strength reduction, f_v, 13 Myr after subduction initiation, for a 5.3 cm/yr convergence rate. Without hydrous strength reduction, the decoupling depth is equal to ~98 km. It strongly decreases with water weakening, and reaches 58 km when f_v=100. Note that the weak zone rheology does not depend on water content. We interpret the shallowing of the interplate decoupling depth as resulting from an enhanced thinning of a weaker overlying lithosphere by the mantle wedge flow, that induces a shallower ductile behavior in a warmer subduction plane (comparison of f_v=1 and f_v=10 cases, Fig. 6a). The decoupling depth becomes progressively shallower

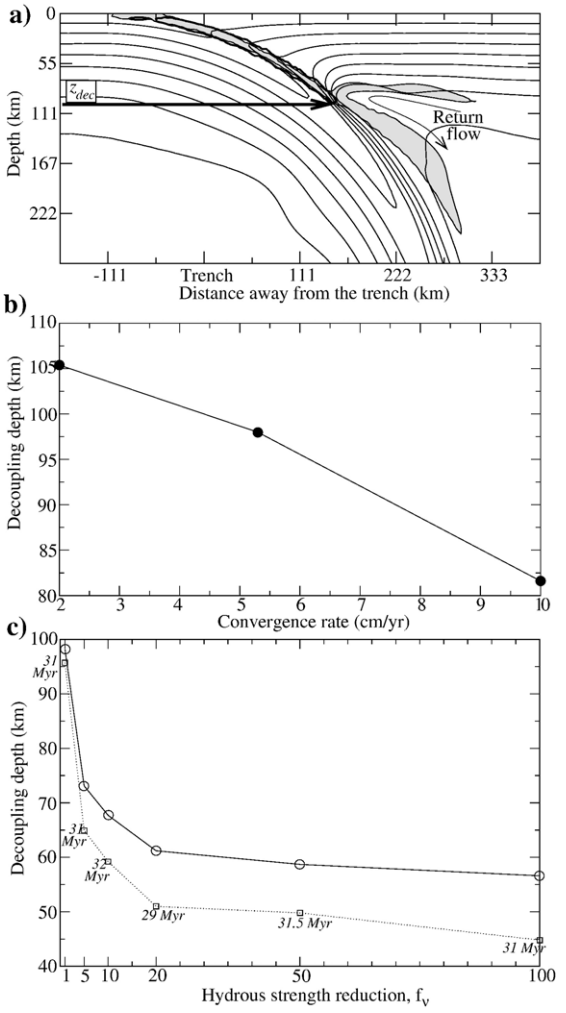

Fig. 7. Panel (a): Zoom on the interplate thermal state and the strain localization area, 13 Myr after subduction initiation, for a simulation without water weakening (f_v=1, simulation S1, Table 2). Isotherms (thin lines) are displayed every 150 °C. The strain rate is maximum in the gray filled area. The thick black line delimits the area where mechanical dissipation rate is greater than 18 μW m^{-3}. The decoupling depth corresponds to a maximum in dissipation energy. Panel (b): Decoupling depth as a function of the subduction velocity, v (simulations S1, S1b, and S1c, Table 2). Panel (c): Decoupling depth as a function of the hydrous strength reduction, f_v (simulations S1, S2 to S6, Table 2). Solid line with circles: 13 Myr after subduction initiation. Dotted line with squares: around 30 Myr after subduction initiation (measured at the time indicated on the plot).

with time, and is close to equilibrium in all cases at ~30 Myr (Fig. 7c). The delay necessary for equilibration of the interplate structure corresponds to the progressive conductive heating of the cold and rigid forearc nose by enhanced wedge flow. In the case of a quite extreme hydrous strength reduction (f_v=100), where the convective warming of the backarc is extremely strong, the decoupling depth reaches 45 km below the surface.

4.3. Consequence of upper lithosphere thinning for the slab thermal state

Thermal profiles across the subducting slab illustrate the thermal state of the slab surface below the volcanic arc. Fig. 6b exhibits the profiles perpendicular to the slab obtained 13 Myr after subduction initiation for simulations performed with f_v=1, 10, and 100 (simulations S1, S3, and S6, Table 2). The profile location is chosen to sample the slab surface temperature at about 90 km depth, corresponding to that of the subducting slab top below the volcanic front (e.g., [66]).

The main difference between thermal profiles is related to the overriding plate thinning for f_v>1 (Fig. 6b). Twenty kilometers away from the slab surface, the maximum temperature is 1260 °C for f_v=10, while it is only 930 °C without water weakening (f_v=1) but while it is also lower, limited to 1140 °C, when upper plate convective erosion occurs (f_v=100). Simple corner flow enhancement (f_v=10) thus implies a warming of the slab surface by enhanced upper plate ablation. On the other hand, for f_v>20, the SST increase is counterbalanced by cold dripping blob advection, due to convectively driven flow. Moreover, the slab top cooling increases with time as upper plate thinning proceeds: 31 Myr after subduction initiation, the temperature 20 km away from the slab surface is further reduced to 1050 °C (f_v=100, Fig. 6b). The convective ablation of the arc lithosphere thus induces two opposite thermal effects. On one hand, it warms the slab surface in the vicinity of the decoupling depth. On the other hand, the cold blobs detached from the overlying plate by convective destabilization cool the slab surface.

Note in Fig. 6 the very strong thermal gradients (between 31.5 °C/km and 44.8 °C/km for simulation S1 to S6) that occur across the subducted crust. An accurate prediction of slab crust and sediment melting is not possible here, as strain does not localize exactly on the crust top but is distributed across a 7 km thick crustal layer. However, we illustrate in the following the thermal evolution of the oceanic crust in our models by P−T paths.

4.4. P−T paths of the subducted oceanic crust

We follow the P−T evolution of a crustal particle, initially located at 3 km depth and 388 km away from the trench at subduction initiation, for simulations S1 to S6 ($1 \le f_v \le 100$, Fig. 8). The P−T path for the reference case (f_v=1, simulation S1) is colder by 100 to 200 °C than that shown in [19] in the same configuration, as it represents a stage of subduction closer to steady state.

Without water weakening effect, the oceanic crust undergoes a steep temperature increase when it reaches the decoupling depth of 95 km (31 kbar, Fig. 8a). If f_v>1, the strong thermal gradient along the crustal P−T path appears at decreasing depths, 24 kbar (73 km), 19 kbar (57 km), and 16 kbar (49 km), respectively, if f_v=5, 10, and 20, respectively, in agreement with the shallowing of interplate decoupling depth (Fig. 7c). Surprisingly, this high thermal gradient is strongly smoothed when convective destabilization of the overriding plate occurs, for $f_v \ge 50$ (Fig. 8b). To understand this result, note that the base of the upper lithosphere, thinned by convection, and the wedge have overall an almost homogeneously low viscosity: The viscosity reduction by water is larger in the cold lithosphere containing hydrous minerals than in the hot wedge dissolving water, and compensates more or less the temperature-dependence of viscosity [19]. Crustal P−T paths for f_v=50 and 100 then approach the relatively cold P−T paths obtained for an isoviscous mantle wedge model [17,67], although convective upper plate thinning and shallow decoupling depth characterize the present simulations but are excluded from the isoviscous models.

In all cases, for depths greater than the deepest decoupling depth obtained here (~100 km), the P−T paths are colder as the upper plate thinning rate increases (as f_v increases). In other words, the cooling effect of the viscous blanket thickening increases with the amount of upper plate ablation. The maximum temperature reduction is about 150 °C (Fig. 8b). Note that, whatever the thinning mechanism of the upper plate, and even when a steady state is reached, the thinned structure of the arc lithosphere can only be sustained if the strong conductive cooling from above due to high thermal gradients is compensated by the removal of the cooled mantle forming the overlying lithosphere base. Therefore, the SST decrease at depths larger than ~100 km is expected to occur as soon as the arc/backarc plate is thinned and the surface heat flow remains steadily high.

At depths shallower than 100 km, the water weakening effect on the crust thermal state is the following: For simple corner flow enhancement (f_v<20), the depth of significant slab surface heating

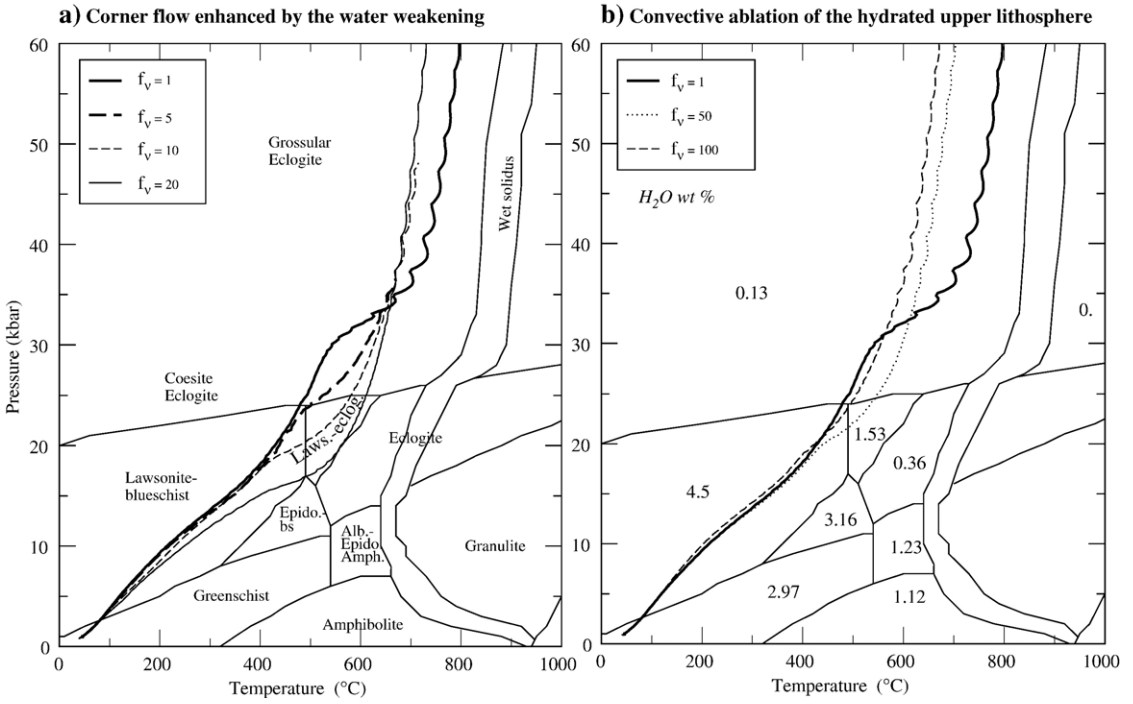

Fig. 8. P−T paths followed by crustal rocks during subduction. Panel (a): Effect of the asthenospheric corner flow enhancement by hydrous strength reduction ($5 \le f_v \le 20$), superimposed on metamorphic facies P−T domains from [47] for a gabbroic crust. Panel (b): influence of convective erosion of the hydrated overriding lithosphere when $f_v > 20$, and water contents in each facies, as computed by [47].

depends on the decoupling depth and corner flow efficiency and decreases with f_v. On the contrary, when $f_v > 20$, the viscous blanket thickening, related to backarc convective ablation, and the decreased focussing of the wedge tip flow, in a nearly isoviscous and very weak wedge, notably cools the slab surface. Finally, these results show that strong upper plate thinning impedes oceanic crust partial melting (Fig. 8).

5. Discussion–conclusion

In the vast majority of mantle wedge flow models, the decoupling depth is prescribed, and fixes the depth of maximum uprising of the return flow, that influences the SST. However, the decoupling depth is expected to derive from a complex thermomechanical equilibrium, mainly depending on (a) the subduction velocity, (b) the mantle wedge rheology and overlying plate stiffness, (c) the friction coefficient on the interplate interface, and (d) crustal phase transitions. We discussed here the influence of (a) and (b). The friction coefficient (c) should also control the interplate decoupling depth as it fixes the stress along the interplate interface. We hypothesize that a higher yield stress should result both in a shallower brittle–ductile transition and in a larger frictional heating along the subduction plane, thus decreasing the interplate decoupling depth. Besides, dehydration reactions inside the subducted crust (d) may increase pore pressure and then reduce frictional strength along the interplate. Note that any increase in interplate frictional strength caused by complete dehydration is not included in our model. Hence, the eclogitization process could partly control the interplate decoupling depth [18]. Our study of the decoupling depth is obviously non exhaustive, however it highlights how the interplate decoupling depth reaches equilibrium depending on the wedge flow, and how it affects the SST.

We show above that the mantle strength is an important parameter controlling the SST, as it strongly affects both the decoupling depth and the upper plate thinning. However, the water effect on rheology is not well known, mainly because of the very broad water content interval encountered in subduction zones (from a few hundreds of ppm to 10% in weight). For a rock dissolving water, the olivine strength is inversely proportional to the water amount [62], and is reduced by about two orders of magnitude at saturation. On the other hand, serpentinization reduces peridotite viscosity by about 4 orders of magnitude at 550 °C and 40 km depth [68,69]. Between these two cases, the behavior of

a hydrated mantle containing ~20 wt.% of amphibole is poorly constrained.

The issue of rheology modelling in wet conditions is further complicated by partial melting, that may occur in the hydrated mantle wedge and affect not only the molten rock strength [60], but also the water distribution in the wedge. To estimate the melting influence on the hydration state within the mantle wedge, we perform a preliminary test by including in the model a batch partial melting parameterization of peridotite under hydrous conditions [70], described in the electronic supplementary material. This test shows that slab dehydration triggers first partial melting of the viscous blanket covering the slab surface. Melt fraction is then quite high (until 30 wt.%) and the water content in the high pressure melt is very large (~30 wt.%). The molten layer above the slab acts as a sponge layer, in which released free water is trapped. However, magma should in these conditions migrate upwards, and loose water during its rising, yielding hydration and possible melting of surrounding rocks.

The effect of melt migration is obtained by limiting the maximum melt fraction retained in the matrix to F_T=3 wt.% [71]. In this model, hydrous partial melting also occurs in the overlying mantle wedge and the upper lithosphere base. The mantle wedge is hydrated and hydrous phases develop at depths shallower than 70 km (along the 980 °C isotherm). Therefore, the water content structure in the subduction zone remains unchanged compared to that simulated without partial melting modelling. Nevertheless, it is clear that the mantle wedge hydration relies on magma migration processes and melt–fluid–rock interactions. Whether melt rises in the wedge mainly by localized flows (e.g., [72–74]), or on the contrary, by distributed porous flow, is likely to affect the mantle wedge hydrous state and, eventually, deformation. Modelling challenges associated with fractional melting parameterization, melt migration processes and melt–fluid–rock interactions are beyond the scope of this study.

Our modelling parameters could be constrained by comparing model predictions to the observed thinning geometry and thinning rates of the upper plate, and to the estimated decoupling depth. The arc lithosphere thinning rate appears in some cases to be particularly high (between 3 and 10 Myr, [11,12,75]), possibly suggesting a strong hydrous strength reduction well within the overriding lithosphere. Three different data sets can be used to investigate the decoupling depth. First, the surface heat flow increase from the trench towards the backarc can be used to quantify the decoupling depth [18]. Second, the vertical transition between high P-wave velocity/low attenuation anomalies (forearc nose) and low velocity/high attenuation domain (asthenosphere) is argued to mark the decoupling depth location [34,25,35]. Third, in cases where estimated P−T paths of subducted sediments or crust display an isobaric heating, the latter should be an indicator of the decoupling depth and the corner flow focussing. In this paper, we emphasize that, in areas where the overriding lithosphere is strongly thinned, the decoupling depth should be shallow and associated with cold P−T path without isobaric heating and without crust/sediment melting.

Acknowledgements

This work was supported by the French national program, DyETI 2004–2006, “Dynamique de la subduction”. We thank two anonymous reviewers for their constructive comments that helped improving the manuscript.

Appendix A. Supplementary data

Supplementary data associated with this article can be found, in the online version, at doi:10.1016/j.epsl.2006.12.027.

References

[1] P. Kelemen, J. Rilling, E. Parmentier, L. Mehl, B.R. Hacker, Thermal structure due to solid-state flow in the mantle wedge beneath arcs, in: J. Eiler (Ed.), Inside the Subduction Factory, Geophys. Monogr. Ser., vol. 138, AGU, Washington, D.C., 2003, pp. 293–311.
[2] B. Marsh, Island-arc volcanism, Am. Sci. 67 (1979) 161–172.
[3] J. Myers, B. Marsh, A. Sihna, Primitive high-Al basalts in Aleutians, Contrib. Mineral. Petrol. 91 (1985) 221–234.
[4] A. Johnston, Anhydrous P–T phase relations of near-primary high alumina basalt from the South Sandwich Islands, Contrib. Mineral. Petrol. 92 (1986) 368–382.
[5] C. Currie, K. Wang, R. Hyndman, J. He, The thermal effects of steady-state slab-driven mantle flow above a subducting plate: the Cascadia subduction zone and backarc, Earth Planet. Sci. Lett. 223 (2004) 35–48.
[6] Y. Tatsumi, M. Sakuyama, H. Fukuyama, I. Hushiro, Generation of arc basalt magmas and thermal structure of the mantle wedge in subduction zones, J. Geophys. Res. 88 (1983) 5815–5825.
[7] K. Bartels, R. Kinzler, T. Grove, High pressure phase relations of primitive high-alumina basalts from Medicine Lake Volcano, Northern California, Contrib. Mineral. Petrol. 108 (1991) 253–270.
[8] D. Draper, A. Johnston, Anhydrous P–T phase relations of an Aleutian high-MgO basalt: an investigation of the role of olivine–liquid reaction in the generation of arc high-alumina basalts, J. Geophys. Res. 112 (1992) 501–519.
[9] T. Sisson, S. Bronto, Evidence for pressure-release melting beneath magmatic arcs from basalt at Galunggung, Indonesia, Nature 391 (1998) 883–886.
[10] L. Elkins Tanton, T. Grove, J. Donnelly-Nolan, Hot, shallow melting under the Cascades volcanic arc, Geology 29 (2001) 631–634.

[11] C. Garrido, I. ChaneFo, J.-L. Bodinier, B. Dhuime, D. Bosh, O. Bruguier, S. Hussain, H. Dawood, J.-P. Burg, Origin of the island arc petrological Moho via melt-rock reaction: Evidence from the Jijal complex (Kohistan complex, N. Pakistan), Geology (submitted for publication).
[12] C.J. Garrido, J.-L. Bodinier, J.-P. Burg, G. Zeilinger, S.S. Hussain, H. Dawood, S. Chaudhry, F. Gervilla, Petrogenesis of mafic garnet granulite in the lower crust of the Kohistan paleo-arc complex (Northern Pakistan): implications for intra-crustal differentiation of island arcs and generation of continental crust, J. Petrol. 47 (2006) 1873–1914.
[13] S. DeBari, R. Coleman, Examination of the deep levels of an island arc: evidence from the Tonsina ultramafic–mafic assemblage, Tonsina, Alaska, J. Geophys. Res. 94 (1989) 4373–4391.
[14] M. Toksöz, J. Minear, B. Julian, Temperature field and geophysical effects of a downgoing slab, J. Geophys. Res. 76 (1971) 1113–1138.
[15] J.H. Davies, D. Stevenson, Physical model of source region of subduction volcanism, J. Geophys. Res. 97 (1992) 2037–2070.
[16] S. Peacock, T. Rushmer, A. Thompson, Partial melting of subducting oceanic crust, Earth Planet. Sci. Lett. 121 (1994) 227–244.
[17] S.M. Peacock, Thermal and pretrologic structure of subduction zones, in: S.H.K. Gray, E. Bebout, David W. Scholl, J.P. Platt (Eds.), Subduction: Top to Bottom, Geophys. Monogr. Ser., vol. 96, AGU, Washington, D.C., 1996, pp. 119–133.
[18] Y. Furukawa, Depth of the decoupling plate interface and thermal structure under arcs, J. Geophys. Res. 98 (1993) 20005–20013.
[19] D. Arcay, E. Tric, M.-P. Doin, Numerical simulations of subduction zones: effect of slab dehydration on the mantle wedge dynamics, Phys. Earth Planet. Inter. 149 (2005) 133–153.
[20] D. Arcay, M.-P. Doin, E. Tric, Overriding plate thinning in subduction zones: Localized convection induced by slab dehydration, Geochem. Geophys. Geosyst. 7 (2006), doi:10.1029/2005GC001061 (eid: Q02007).
[21] R. Hassani, D. Jongmans, J. Chéry, Study of plate deformation and stress in subduction processes using two-dimensional numerical models, J. Geophys. Res. 102 (1997) 17951–17965.
[22] S. Honda, M. Saito, T. Nakakuki, Possible existence of small-scale convection under the back-arc, Geophys. Res. Lett. 29 (2002), doi:10.1029/2002GL015853.
[23] S. Honda, M. Saito, Small-scale convection under the back-arc occurring in the low viscosity wedge, Earth Planet. Sci. Lett. 216 (2003) 703–715.
[24] S. Honda, T. Yoshida, Application of the model of small-scaleconvection under the island arc to the NE Honshu subduction zone, Geochem. Geophys. Geosyst. 6 (2005), doi:10.1029/2004GC000785.
[25] J. Conder, A case for hot slab surface temperatures in numerical viscous flow models of subduction zones with an improved fault zone parameterization, Phys. Earth Planet. Inter. 149 (2005) 155–164.
[26] V. Solomatov, L.-N. Moresi, Three regimes of mantle convection with non-Newtonian viscosity and stagnant lid convection on the terrestrial planets, Geophys. Res. Lett. 24 (1997) 1907–1910.
[27] C. Kincaid, I. Sacks, Thermal and dynamical evolution of the upper mantle in subduction zones, J. Geophys. Res. 102 (1997) 12,295–12,315.
[28] S. Zhong, M. Gurnis, Mantle convection with plates and mobile, faulted plate margins, Science 267 (1995) 838–843.
[29] S. Zhong, M. Gurnis, L. Moresi, Role of faults, nonlinear rheology, and viscosity structure in generating plates from instantaneous mantle flow models, J. Geophys. Res. 103 (1998) 15255–15268.
[30] J. van Hunen, A. van der Berg, N. Vlaar, A thermomechanical of horizontal subduction below an overriding plate, Earth Planet. Sci. Lett. 182 (2000) 157–169.
[31] P. van Keken, B. Kiefer, S. Peacock, High-resolution models of subduction zones: implications for mineral dehydration reactions and the transport of water into the deep mantle, Geochem. Geophys. Geosyst. 3 (2002), doi:10.1029/2001GC000256.
[32] A. Rowland, J.H. Davies, Buoyancy rather than rheology controls the thickness of the overriding lithosphere in subduction zones, Geophys. Res. Lett. 26 (1999) 3037–3040.
[33] M. Eberle, O. Grasset, C. Sotin, A numerical study of the interaction between the mantle wedge, the subducting slab, and overriding plate, Phys. Earth Planet. Inter. 134 (2002) 191–202.
[34] E. Kneller, P. van Keken, S. Karato, J. Park, B-type olivine fabric in the mantle wedge: insights from high-resolution non-Newtonian subduction zone models, Earth Planet. Sci. Lett. 237 (2005) 781–797.
[35] G. Abers, P. van Keken, E. Kneller, A. Ferris, J. Stachnick, The thermal structure of subduction zones constrained by seismic imaging: slab dehydration and wedge flow, Earth Planet. Sci. Lett. 241 (2006) 387–397.
[36] Y. Furukawa, Magmatic processes under arcs and formation of the volcanic front, J. Geophys. Res. 98 (1993) 8309–8319.
[37] S. Peacock, R. Hyndman, Hydrous minerals in the mantle wedge and the maximum depth of subduction thrust earthquakes, Geophys. Res. Lett. 26 (1999) 2517–2520.
[38] S. Honda, Thermal structure beneath Tohoku, northeast Japan — a case study for understanding the detailed thermal structure of the subduction zone, Tectonophysics 112 (1985) 69–102.
[39] A. Davaille, C. Jaupart, Transient high-Rayleigh number thermal convection with large viscosity variations, J. Fluid Mech. 253 (1993) 141–166.
[40] C. Dumoulin, M.-P. Doin, L. Fleitout, Heat transport in stagnant lid convection with temperature- and pressure-dependent Newtonian or non-Newtonian rheology, J. Geophys. Res. 104 (1999) 12759–12778.
[41] V. Solomatov, L.-N. Moresi, Scaling of time-dependent stagnant lid convection: application to small-scale convection on Earth and other terrestrial planets, Geophys. Res. Lett. 105 (2000) 21,795–21,817.
[42] U.R. Christensen, Convection with pressure- and temperature-dependent non-Newtonian rheology, Geophys. J. R. Astron. Soc. 77 (1984) 343–384.
[43] U.R. Christensen, An Eulerian technique for thermomechanical modeling, J. Geophys. Res. 97 (1992) 2015–2036.
[44] P. van Keken, S. King, H. Schmeling, U. Christensen, D. Neumeister, M.-P. Doin, A comparison of methods for the modeling of thermochemical convection, J. Geophys. Res. 102 (1997) 22477–22495.
[45] M.-P. Doin, P. Henry, Subduction initiation and continental crust recycling: the roles of rheology and eclogitization, Tectonophysics 342 (2001) 163–191.
[46] M. Schmidt, S. Poli, Experimentally based water budgets for dehydrating slabs and consequences for arc magma generation, Earth Planet. Sci. Lett. 163 (1998) 361–379.
[47] R. Bousquet, B. Goffé, P. Henry, X. Le Pichon, C. Chopin, Kinematic, thermal and petrological model of the Central Alps: Lepontine metamorphism in the upper crust and eclogitisation of the lower crust, Tectonophysics 273 (1997) 105–127.
[48] S.M. Peacock, Fluid processes in subduction zones, Science 248 (1990) 329–337.
[49] K. Seifert, D. Brunotte, Geochemistry of the serpentinized mantle peridotite from site 897, in: R.W., et al., (Eds.), Proceedings of

the Ocean Drilling Program, Scientific Results, vol. 149, Ocean Drilling Program, College Station, Tex., 1996, pp. 603–615.
[50] H. Dick, J. Natland, J. Alt, W. Bach, D. Bideau, J. Gee, S. Haggas, J. Hergoten, G. Hirth, P. Holm, A long in situ section of the lower oceanic crust: results of ODP Leg 176 drilling at the Southwest Indian Ridge, Earth Planet. Sci. Lett. 179 (2000) 31–51.
[51] J. Alt, D. Teagle, Hydrated subducted crust at 100–250 km depth, Earth Planet. Sci. Lett. 176 (2000) 323–330.
[52] S.M. Peacock, Are the lower planes of double seismic zones caused by serpentine dehydration in subducting oceanic mantle? Geology 29 (2001) 299–302.
[53] C. Ranero, J. Phipps Morgan, K. McIntosh, C. Reichert, Bending-related faulting and mantle serpentinization at the Middle America trench, Nature 425 (2003) 367–373.
[54] D. Bell, G. Rossman, Water in Earth's mantle: the role of nominally anhydrous minerals, Science 255 (1992) 1391–1397.
[55] B. Jamtveit, R. Brooker, K. Brooks, L. Larsen, T. Pedersen, The water content of olivines from the North Atlantic Volcanic Province, Earth Planet. Sci. Lett. 186 (2001) 401–415.
[56] A. Peslier, J. Luhr, J. Post, Low water contents in pyroxenes from spinel–peridotites of the oxidized, sub-arc mantle wedge, Earth Planet. Sci. Lett. 201 (2002) 69–86.
[57] D. Kohlstedt, B. Evans, S. Mackwell, Strength of the lithosphere: constraints imposed by laboratory experiments, Contrib. Mineral. Petrol. 123 (1996) 345–357.
[58] R. Lu, H. Keppler, Water solubility in pyrope to 100 kbar, Contrib. Mineral. Petrol. 129 (1997) 35–42.
[59] M. Rauch, H. Keppler, Water solubility in orthopyroxene, Contrib. Mineral. Petrol. 143 (2002) 525–536.
[60] S. Mei, W. Bai, T. Hiraga, D. Kohlstedt, Influence of melt on the creep behavior of olivine-basalt aggregates under hydrous conditions, Earth Planet. Sci. Lett. 201 (2002) 491–507.
[61] D. Turcotte, G. Schubert, Geodynamics: Applications of Continuum Physics to Geological Problems, John, New York, 1982.
[62] G. Hirth, D. Kohlstedt, Water in the oceanic upper mantle: implications for rheology, melt extraction and the evolution of the lithosphere, Earth Planet. Sci. Lett. 144 (1996) 93–108.
[63] S. Mei, D. Kohlstedt, Influence of water on plastic deformation of olivine aggregates. 2. Dislocation creep regime, J. Geophys. Res. 105 (2000) 21,471–21,481.
[64] M. Drury, R. Vissers, D. van der Wal, E. Hoogerduijn Strating, Shear localisation in upper mantle peridotites, Pure Appl. Geophys. 137 (1991) 439–460.
[65] U. Altenberger, Strain localization mechanisms in deep-seated layered rocks, Geol. Rundsch. 86 (1997) 56–68.
[66] P. England, R. Engdahl, W. Thatcher, Systematic variation in the depths of slabs beneath arc volcanoes, Geophys. J. Int. 156 (2004) 377–408.
[67] H. Iwamori, Transportation of H_2O and melting in subducting zones, Earth Planet. Sci. Lett. 160 (1998) 65–80.
[68] M. Toriumi, Flow under the island arc of Japan and lateral variation of magma chemistry of Island arc volcanoes, J. Phys. Earth 26 (1978) 423–435.
[69] J. Escartìn, G. Hirth, B. Evans, Nondilatant brittle deformation of serpentinites: implications for Mohr–Coulomb theory and the strength of faults, J. Geophys. Res. 102 (1997) 2897–2913.
[70] R. Katz, M. Spiegelman, C. Langmuir, A new parameterization of hydrous mantle melting, Geochem. Geophys. Geosyst. 4 (2003) 2002GC000433.
[71] G. Gaetani, T. Grove, Experimental constraints on melt generation in the mantle wedge, in: J. Eiler (Ed.), Inside the Subduction Factory, Geophys. Monogr. Ser., vol. 138, AGU, Washington, D.C., 2003, pp. 107–134.
[72] M. Spiegelman, P. Kelemen, E. Aharonov, Causes and consequences of flow organization during melt transport: the reaction infiltration instability in compactible media, J. Geophys. Res. 106 (2001) 2061–2077.
[73] B. Holtzman, N. Groebner, M. Zimmerman, S. Ginsberg, D. Kohlstedt, Stress-driven melt segregation in partially molten rocks, Geochem. Geophys. Geosyst. 4 (2003), doi:10.1029/2001GC000258.
[74] T. Gerya, D. Yuen, Rayleigh–Taylor instabilities from hydration and melting propel 'cold plumes' at subduction zones, Earth Planet. Sci. Lett. 212 (2003) 47–62.
[75] C. Garzione, P. Molnar, J. Libarkin, B. MacFadden, Rapid late Miocene rise of the Bolivian Altiplano: evidence for removal of mantle lithosphere, Earth Planet. Sci. Lett. 241 (2005) 543–556.